



**Politecnico
di Torino**

Automotive Engineering

A.Y. 2024/2025

Car body design and aerodynamics

Aerodynamics Reports

Student:

Walter Maggio (S343988)

Contents

1 Mito CFD analysis	1
1.1 Introduction	1
1.2 CFD Workflow	1
1.2.1 Geometry Preparation	1
1.2.2 Mesh Generation	2
1.2.3 Physics Setup	3
1.2.4 Post-Processing	4
1.3 Results and Discussion	5
1.3.1 Aerodynamic Coefficients	5
1.3.2 Flow Field Analysis	6
1.4 Conclusion	8
2 Mito CFD post-processing	10
2.1 Introduction	10
2.2 CFD Workflow	10
2.2.1 Simulation Setup	10
2.3 Results and Discussion	12
2.3.1 Aerodynamic Coefficients	12
2.3.2 Accumulated aerodynamic force	13
2.3.3 Flow Field Analysis	14
2.4 Comparison with Wind Tunnel Data	17
2.5 Conclusion	17

Report 1

Mito CFD analysis

1.1 Introduction

Aerodynamic performance plays a crucial role in determining the efficiency and stability of modern vehicles. This report presents a detailed Computational Fluid Dynamics (CFD) analysis of the Alfa Romeo MiTo. The primary focus of the study is to assess the aerodynamic coefficients: drag coefficient (C_D) and lift coefficient (C_L), using STAR-CCM+ software. The analysis contain the entire CFD workflow, including geometry preparation, meshing, physics setup, simulation execution, and results validation. The findings are then compared with experimental wind tunnel data to evaluate the reliability of the CFD model.

The objectives of this analysis are:

- Quantify the aerodynamic coefficients of the Alfa Romeo MiTo under specified conditions.
- Visualize and interpret the flow fields around the vehicle to identify areas contributing to drag and lift.
- Investigate discrepancies between CFD results and experimental data to improve the simulation methodology.

1.2 CFD Workflow

1.2.1 Geometry Preparation

The foundation of any CFD analysis lies in the preparation of the geometry. For this study, the Alfa Romeo MiTo geometry was provided as a triangulated surface mesh file, `Mito-half-ex1.inp`. Utilizing a half-domain model reduces computational effort by leveraging symmetry. Key steps in this phase included:

1. **Importing Geometry:** The surface mesh was imported into STAR-CCM+. The provided geometry was checked to ensure it was watertight, with no penetrations or triple edges that could disrupt meshing.
2. **Setting Symmetry Plane:** A symmetry boundary condition was applied to halve the computational domain. This not only reduced computational cost but also maintained the accuracy of the analysis, given the vehicle's nearly symmetrical design.
3. **Validation:** Tools within STAR-CCM+ were used to inspect the geometry for errors such as non-manifold edges and free edges. Any issues identified were resolved through surface repair techniques.

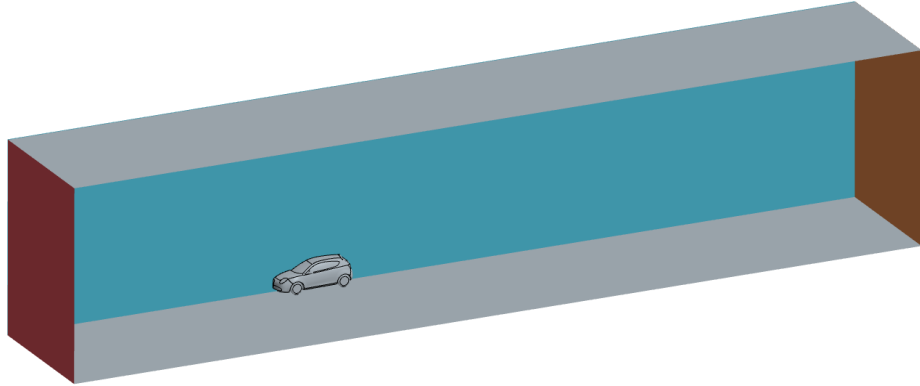


Figure 1.1: Car and wind tunnel imported model

By the end of this phase, the geometry was validated and ready for the meshing process.

1.2.2 Mesh Generation

Mesh quality is a critical determinant of simulation accuracy. The meshing process was carried out using STAR-CCM+'s automated meshing tools, which offer a balance between precision and efficiency. The following parameters and strategies were implemented:

1. **Base Mesh Settings:**
 - Base size: 25 mm, ensuring sufficient resolution for the entire domain.
 - Automated meshing operations enabled: Surface remesher, polyhedral mesher, and prism layer mesher.
2. **Boundary Layer Meshing:**
 - Prism layer near-wall thickness: 2 mm.

- Total prism layer thickness: 10 mm.
- Three layers were created to capture the high velocity and pressure gradients near the vehicle's surface.

3. Refinements in Critical Regions:

- Specific regions, such as the spoiler, mirrors, and wake areas, were assigned custom surface and volumetric controls. For instance, the VR-spoiler region was refined with a target mesh size of 75 % of the base size.

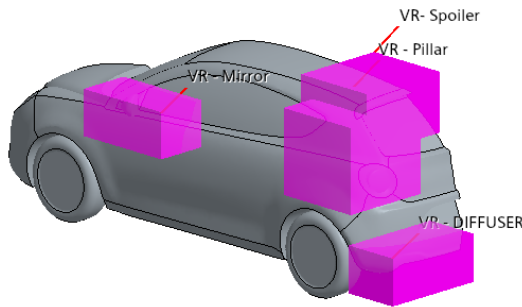


Figure 1.2: Boxes to execute a mesh refinement

- ### 4. Mesh Validation:
- A total cell count of approximately 500,000 was achieved. The mesh was inspected for uniformity, and problematic areas were corrected before proceeding.

This phase concluded with a high-quality mesh that balanced computational efficiency and resolution.

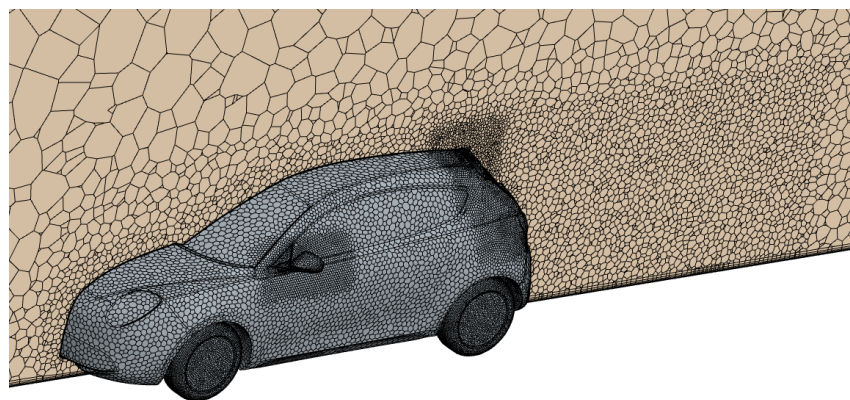


Figure 1.3: Generated mesh for the model

1.2.3 Physics Setup

The next step involved configuring the physics models to simulate the flow around the vehicle accurately. The following settings were applied:

1. Simulation Type:

- Steady-state, three-dimensional (3D), incompressible flow.
- The Reynolds-Averaged Navier-Stokes (RANS) approach was selected due to its computational efficiency for steady flows.

2. Fluid Properties:

- Air was modeled as an incompressible fluid with a density of 1.225 kg/m^3 and a dynamic viscosity of $1.79 \times 10^{-5} \text{ Pa}\cdot\text{s}$.

3. Boundary Conditions:

- **Inlet:** Velocity inlet condition set to 38.89 m/s (140 km/h).
- **Outlet:** Pressure outlet condition set to 0 Pa.
- **Walls:** Vehicle surfaces were treated as no-slip walls, while tunnel walls were assigned slip conditions to emulate wind tunnel behavior.

4. Turbulence Model:

The $k-\epsilon$ turbulence model was chosen due to its robustness and efficiency for high-Reynolds-number flows. While not ideal for capturing intricate flow separation, it provides a reasonable approximation for this application.

5. Solver Settings:

- Relaxation factors: Default values (e.g., velocity = 0.7, pressure = 0.3) ensured stability during convergence.
- Stopping criteria: A maximum of 700 iterations was set, with residuals monitored for convergence (target: residuals $< 10^{-3}$).

1.2.4 Post-Processing

Post-processing focused on extracting meaningful insights from the simulation. The following tasks were carried out:

1. **Aerodynamic Coefficients:** Drag and lift coefficients (C_D and C_L) were computed.

2. Flow Field Visualization:

- Scalar displays were created to visualize pressure coefficients, velocity fields, and streamlines.
- Areas of flow separation and wake regions were identified and analyzed in detail.

3. Validation Against Experimental Data:

Results were compared to experimental wind tunnel data to assess the simulation's accuracy.

1.3 Results and Discussion

1.3.1 Aerodynamic Coefficients

The computed aerodynamic coefficients were:

- Drag Coefficient (C_D): 0.283.
- Lift Coefficient (C_L): -0.063

Experimental data provided by CRF for the Alfa Romeo MiTo at 140 km/h indicated:

- $C_D = 0.290$
- $C_L = 0.100$.

The discrepancies observed between the CFD and experimental results were relatively minor concerning the aerodynamic drag coefficient. However, significant differences emerged in the evaluation of the lift coefficient. The CFD results indicate a negative value, whereas the experimental data reveal quantify a positive lift coefficient.

These discrepancies can be attributed to the considerable simplifications made to the CFD model. For instance, the underbody was modeled as a flat floor, omitting all discontinuities and complex geometrical features present in the actual vehicle. Additionally, on the upper body, details such as wipers were removed, and all cavities were closed, further diverging from the real-world geometry.

An analysis of the accumulated force along the vehicle profile (Figure 2.4) reveals that the majority of the aerodynamic drag is generated in the rear portion of the car, primarily due to the wake region. Additionally, significant drag is produced in the frontal section of the body and in the area around the side mirrors. Conversely, the windshield region exhibits an aerodynamic drag recovery, contributing to a reduction in overall drag.

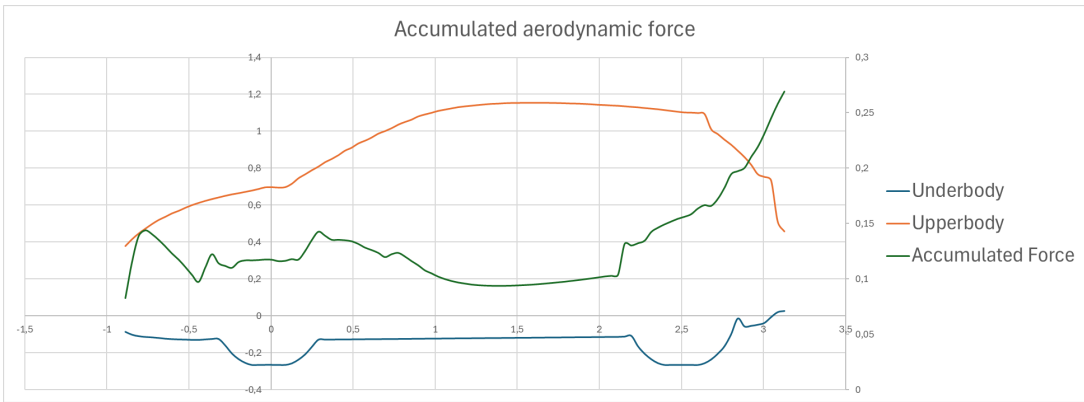


Figure 1.4: Accumulated force along the vehicle profile

1.3.2 Flow Field Analysis

1. Pressure Distribution:

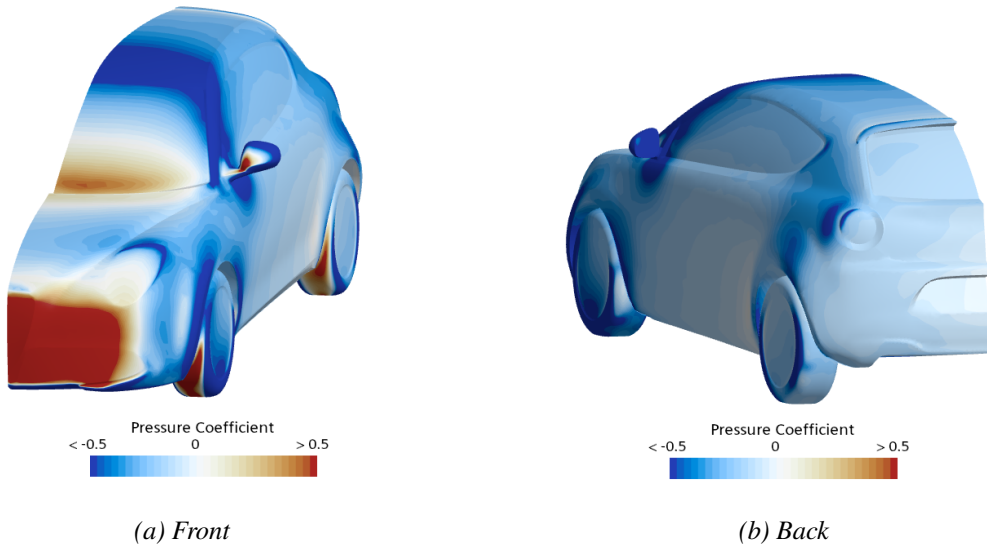


Figure 1.5: Pressure coefficient along the vehicle surface

- High-pressure regions were observed at the vehicle's front and side mirror frontal surface, contributing significantly to drag.
- The wheels are highly exposed to the airflow, resulting in elevated pressure coefficient values. This exposure significantly contributes to the overall increase in the drag coefficient.
- Low-pressure zones at the rear caused flow separation, resulting in a prominent wake.

2. Velocity Field:

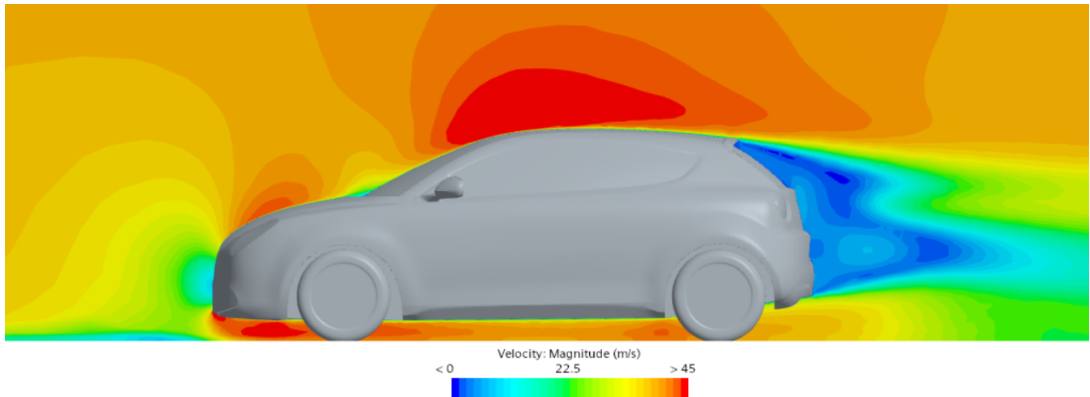


Figure 1.6: Velocity field around the body shape

- Behind the vehicle, a wake region characterized by a low-velocity field is observed, which generates the majority of the vehicle's drag. From this perspective, the detachment of airflow from the body appears to be well-managed.
- The boundary layer development along the underbody aligns with expected behavior, given the geometric simplifications in this region. High-velocity flow is observed beneath the car; however, it is can be attributable to the geometrical simplification of the underbody because the flat floor does not slow down the air flow as a complex surface.

3. Streamlines:

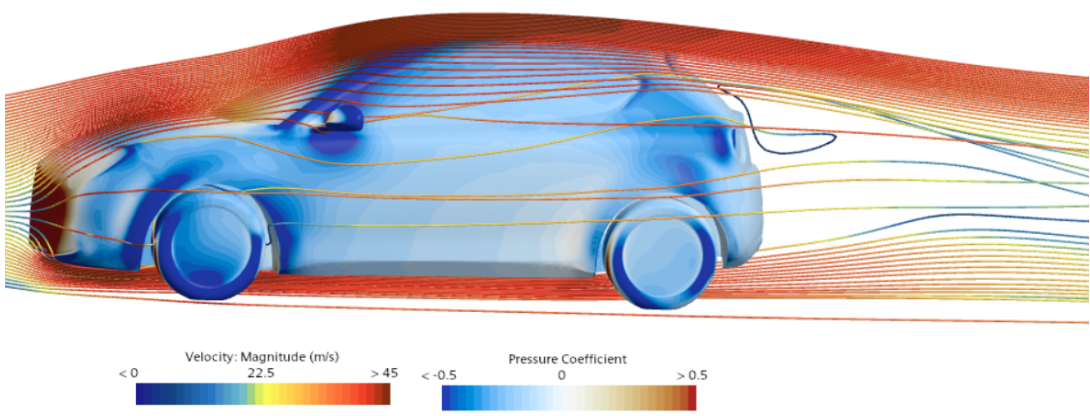


Figure 1.7: Streamlines around the body of the vehicle

- An analysis of the flow behavior around the vehicle's body reveals that the detachment of the flow in the rear section is not well-managed near the rear headlights. Specifically, the flow tends to adhere to the rear hood, contributing to increased

turbulence in the wake region. This phenomenon is particularly evident in Figure 1.8b.

4. Pressure isosurface:

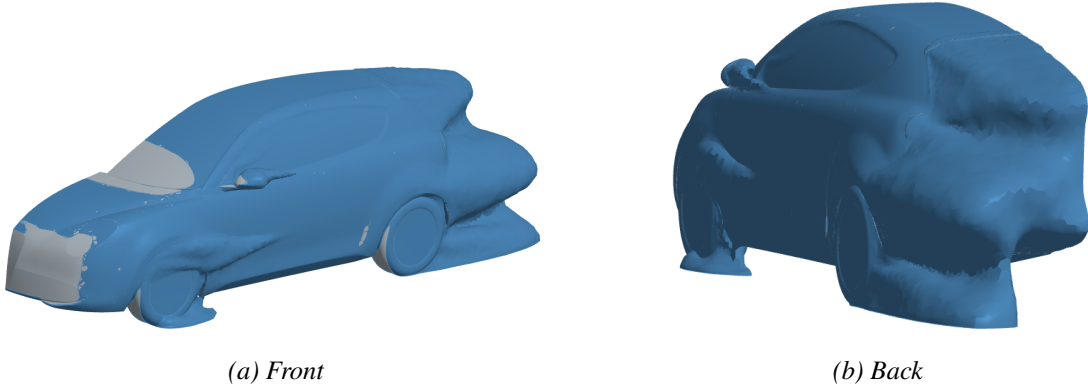


Figure 1.8: Isosurface

- As previously discussed, the improper detachment of the flow near the rear headlight area is evident. This behavior disrupts the uniformity of the wake region, contributing to increased turbulence and aerodynamic inefficiency.
- A wake region is also generated by the side mirrors, which significantly contribute to the overall drag coefficient. Additionally, the flow detachment in this area impacts the downstream airflow, exacerbating aerodynamic losses.
- The front wheels and their wheel arches induce flow separation both above and below these components. This separation further adds to the aerodynamic drag and affects the stability of the boundary layer around the vehicle.

1.4 Conclusion

In conclusion the drag coefficient (C_x) obtained from the CFD simulation was in close agreement with experimental data, demonstrating the reliability of the CFD approach in estimating drag. However, significant discrepancies were observed in the lift coefficient, with the CFD simulation predicting a negative value ($C_L = -0.063$), contrary to the experimental result ($C_L = 0.1$). These differences can be attributed to the simplifications in the CFD model, including the flat underbody and the omission of features such as wipers and open cavities, which play a critical role in real-world flow behavior. Summarizing, the shape simplification negatively affect the estimation of lift coefficient, however, allow to estimate correctly the drag coefficient,

Regarding the flow field characterization, the wake region behind the vehicle emerged as a major contributor to drag, driven by low-velocity, turbulent flow. The detachment of airflow in this region was largely consistent with expectations but showed localized inefficiencies near the rear headlights and hood, where turbulence was more pronounced. Additionally, areas around the side mirrors and front wheels exhibited significant flow separation, increasing drag. The windshield area, however, demonstrated aerodynamic recovery, partially mitigating drag forces.

Report 2

Mito CFD post-processing

2.1 Introduction

The primary objective of this study was to evaluate the effect of a geometric modification (the addition of front wheel spat) on the aerodynamic performance of the Alfa Romeo MiTo. The study compares two configurations:

- **Baseline:** Vehicle without front wheel spats.
- **Modified:** Vehicle with front wheel spats.

The focus of the analysis is on the variation in the drag coefficient (ΔC_D) due to the modification, supported by a detailed flow field characterization to understand the involved aerodynamic phenomena. Simulations were conducted under the following conditions:

- Vehicle speed: 140 km/h.
- Ride height: EADE configuration.
- RRS (Rolling Road Simulation).

The results from the CFD simulations are validated against wind tunnel data, providing a comprehensive understanding of the aerodynamic implications of the modification.

2.2 CFD Workflow

2.2.1 Simulation Setup

The simulations were performed using STAR-CCM+. The workflow follow the following steps:

- **Mesh Preparation**

A trimmed mesh with prism layers was used to accurately capture the boundary layer effects. Refinements were applied to critical regions, including:

- Front wheels and their wake.
- Vehicle underbody.
- Rear wake region.

The mesh ensured a balance between computational efficiency and solution accuracy, resulting in a total cell count optimized for high-resolution results.

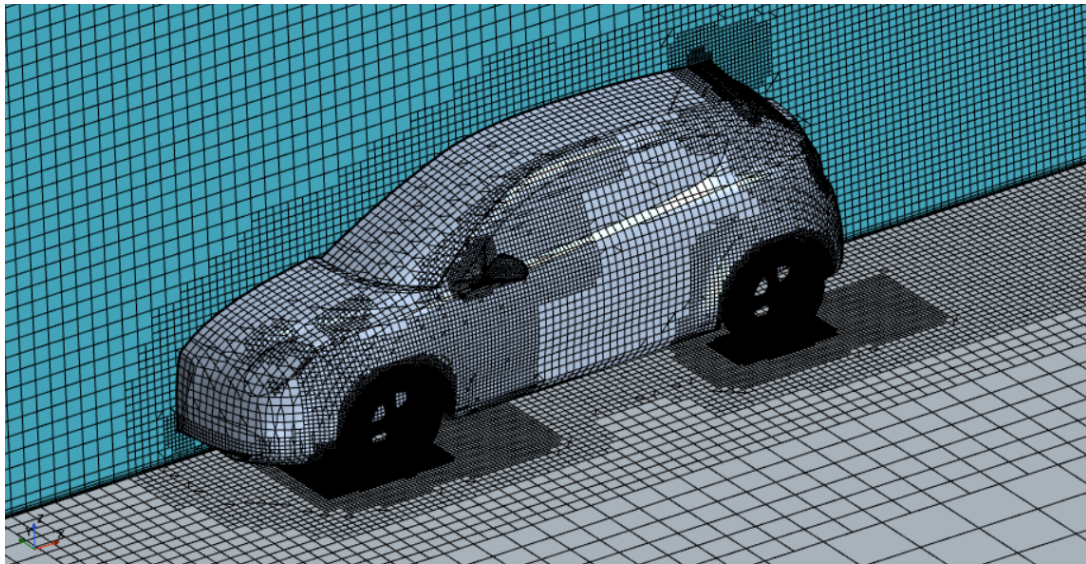


Figure 2.1: Mesh of the model

- **Boundary Conditions**

Boundary conditions were defined as follows:

- **Rotating Wheels:** Tangential velocity boundary conditions and a Moving Reference Frame (MRF) were applied to simulate realistic wheel motion.
- **Moving Ground Plane:** Simulated to replicate real-world driving conditions.
- **No-slip Walls:** Applied to all other boundaries.

- **Physics Setup**

The physics model employed:

- Steady-state, incompressible flow.
- Reynolds-Averaged Navier-Stokes (RANS) equations.

- $k-\epsilon$ turbulence model for robust and efficient simulation of high-Reynolds-number flows.

- **Convergence Monitoring**

Convergence of the numerical solution was monitored using:

- Residual plots: Acceptable convergence achieved at residuals $< 10^{-3}$.

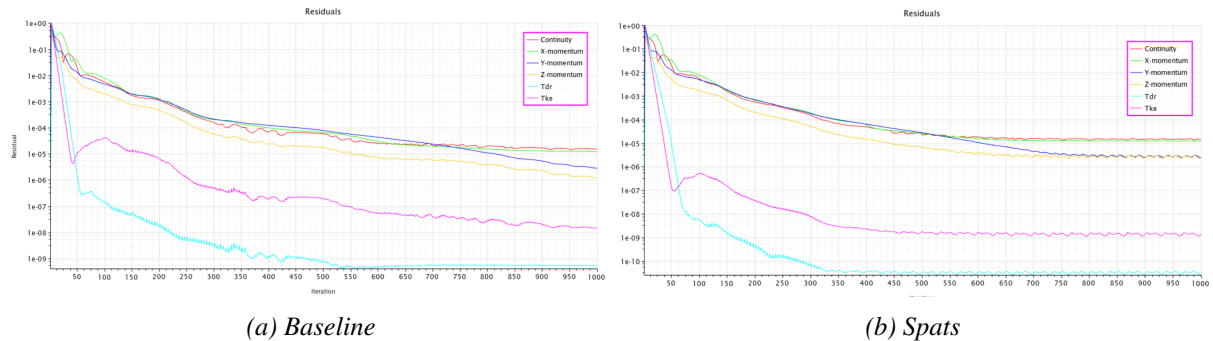


Figure 2.2: Residuals during iterations

- Drag coefficient stability: Checked through force monitor plots to ensure steady-state convergence.

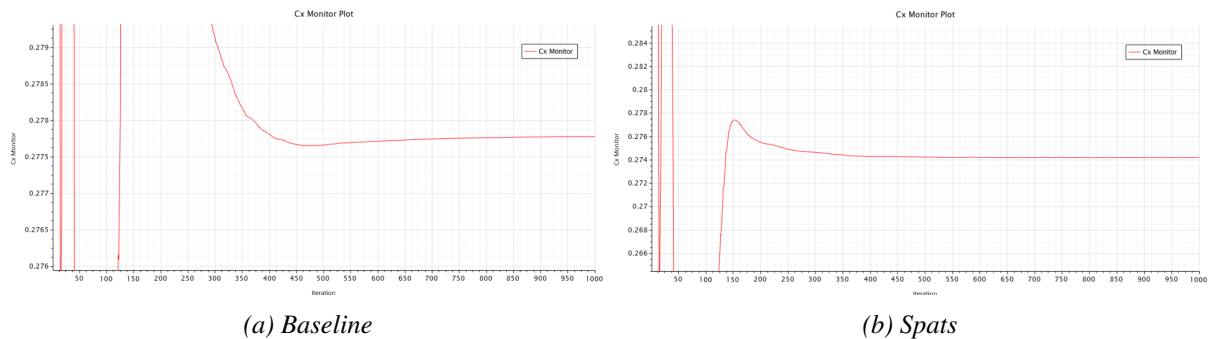


Figure 2.3: Residuals during iterations

2.3 Results and Discussion

2.3.1 Aerodynamic Coefficients

The drag coefficient (C_D) values for both configurations were computed averaging the last 100 iterations, the results are summarized below:

- **Baseline Configuration (No Spats):** $C_D = 0.278$.
- **Modified Configuration (With Spats):** $C_D = 0.274$.

- **Drag Reduction (ΔC_D):** -0.004 .

The results indicate a measurable reduction in drag due to the addition of front wheel spats. This improvement is slightly lower than wind tunnel data, which reported a ΔC_D of -0.006 . However, in both case, the spats effectively leading to enhanced aerodynamic performance.

2.3.2 Accumulated aerodynamic force

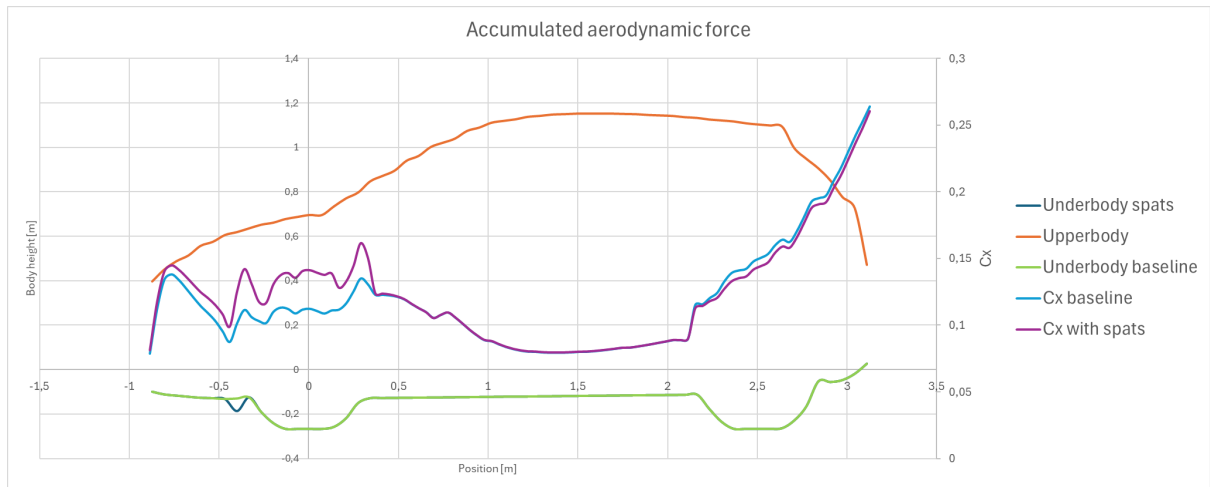


Figure 2.4: Accumulated aerodynamic force along the vehicle profile

The analysis reveals that the baseline configuration exhibits a lower accumulated aerodynamic force in the frontal section of the body, with a noticeable difference compared to the modified version. The effects of the front wheel spats become particularly evident in the rear portion of the frontal wheel arch, where the modified configuration demonstrates a more substantial drag recovery than the baseline (evident in figure 2.6). Further along the vehicle profile, both configurations exhibit comparable aerodynamic behavior until the rear wheel, where the interaction of airflow with the wheel generates a slightly lower amount of drag in the modified configuration.

2.3.3 Flow Field Analysis

- Pressure Coefficient (C_p) Distribution

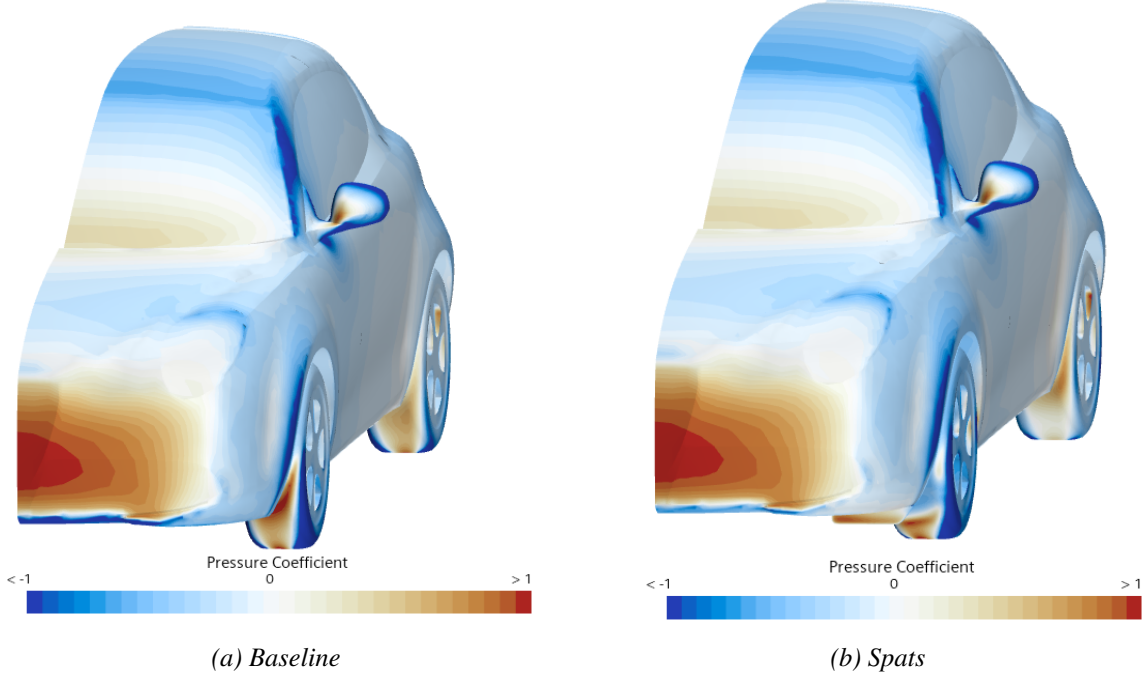


Figure 2.5: Pressure coefficient evaluate on the vehicle surface

The addition of front wheel spats significantly reduces the amount of pressure generated on the front wheels. However, this comes with the trade-off of creating a high-pressure zone on the surface of the spats, which contributes to an increase in drag. Furthermore, the presence of spats slightly reduces the pressure on the rear wheels, which plays a key role in the observed drag improvement between the two configurations.

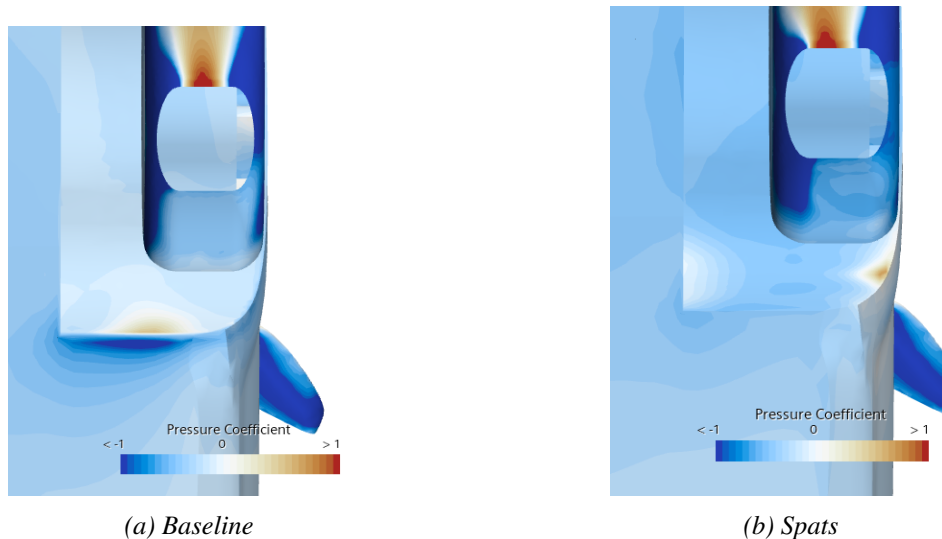


Figure 2.6: Pressure coefficient evaluate on the rear portion of frontal wheel arch

As mentioned previously (paragraph 2.3.2), a substantial drag recovery is observed in the rear section of the front wheel arch due to the lower pressure on its surface when spats are incorporated. In addition, the configuration with spats shows slightly lower pressure on the underbody in the zone around the wheel arc.

- **Velocity Field**

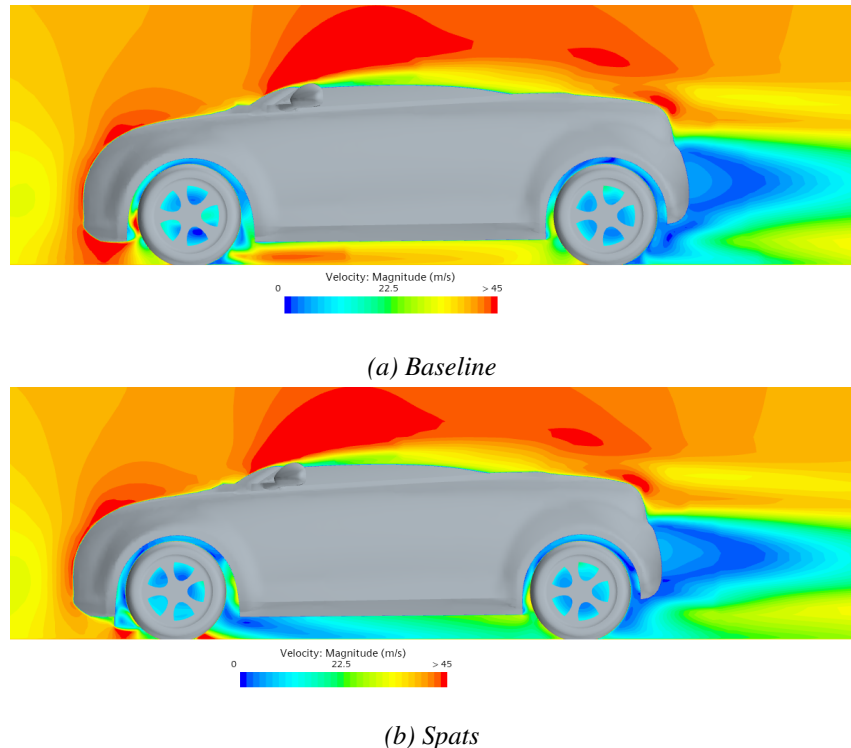


Figure 2.7: Velocity field on the side view of the vehicle

Significant differences are observed in the wake region behind the rear wheel, where the configuration with spats exhibits a noticeably reduced wake. Additionally, the flow beneath the underbody varies drastically between the two configurations. The baseline version displays a moderately high-velocity flow, whereas the version with spats demonstrates a lower-velocity flow in this region.

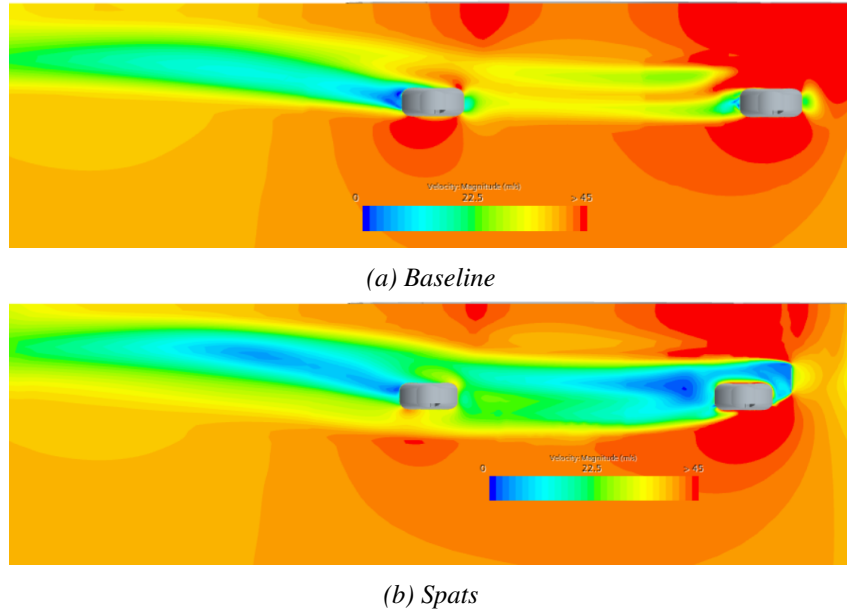


Figure 2.8: Velocity field on the bottom view of the vehicle

As previously mentioned, this observation is clearly illustrated in Figure 2.8, which highlights how the addition of spats generates a significantly larger low-velocity field compared to the baseline configuration. This phenomenon translates into higher pressure in the underbody when spats are used, leading to a substantial reduction in the downforce generated ($\Delta C_L = -0.154$).

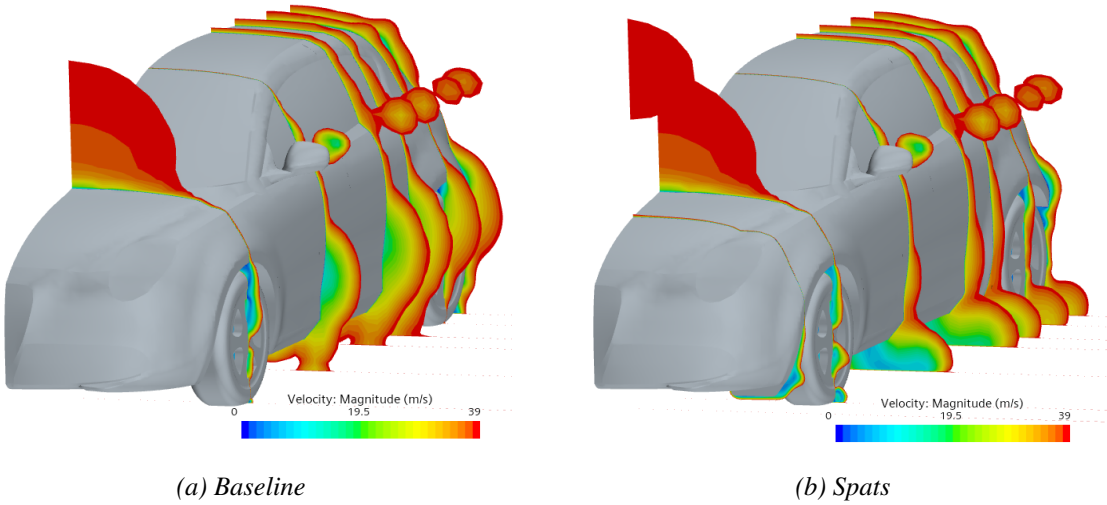


Figure 2.9: Velocity field on frontal planes clipped at 39 m/s

In the configuration without spats, significant flow detachment is observed along the side surface of the vehicle, primarily caused by the front wheel. This phenomenon is drastically reduced when spats are used. As illustrated in Figure 2.9b, the flow remains

better attached to the side surface of the body, and the wake region becomes smaller and shifts toward the underbody.

- **Streamlines and Wake Visualization**

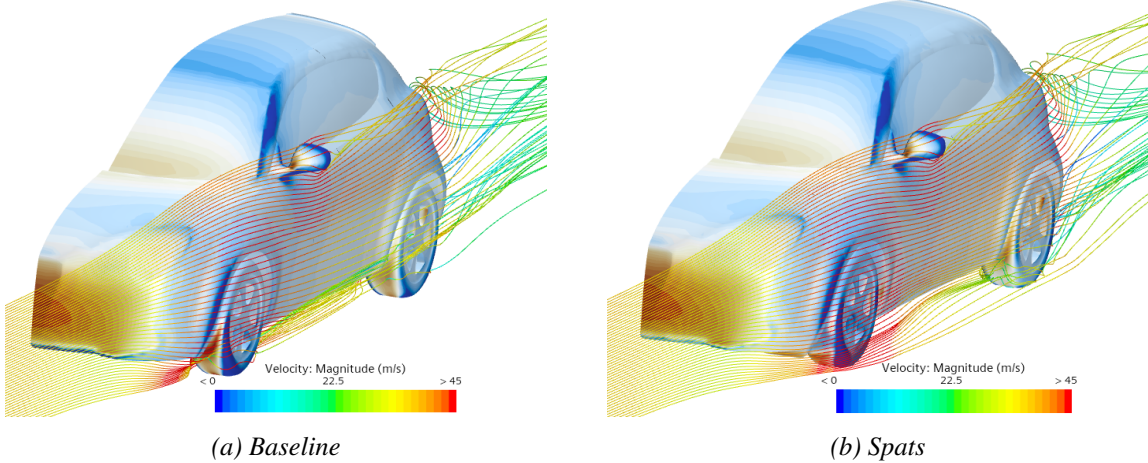


Figure 2.10: Streamlines visualization colored using velocity magnitude

From these images, it is easy to understand the outwash effect generated by the spats. In the baseline configuration, the airflow tends to impact the front wheel directly. In contrast, in the improved version with spats, the airflow is diverted behind the wheel and directed toward the side of the vehicle, reducing drag and improving aerodynamic efficiency.

2.4 Comparison with Wind Tunnel Data

The wind tunnel tests conducted under identical conditions reported a ΔC_D of -0.006 , which is slightly different from the value extracted from the CFD simulation (ΔC_D of -0.006). This small discrepancy can be attributed to the evident geometrical simplifications of the CFD model. However, despite these simplifications, the CFD simulation is able to provide an accurate representation of real-world aerodynamic behavior, offering valuable insights into the effects of the geometric modifications.

2.5 Conclusion

In conclusion, the addition of spats demonstrated measurable improvements in aerodynamic resistance, validated by both simulation and wind tunnel data.

Findings can be summarized as follow:

- **Drag Coefficient Reduction:**

The addition of spats reduced the drag coefficient by $\Delta C_D = -0.004$ in the CFD simulations, closely aligning with wind tunnel results ($\Delta C_D = -0.006$).

This reduction is attributed to the spats' ability to divert airflow away from the front wheels, minimizing direct pressure and turbulence in the wheel region.

- **Flow Characteristics:**

The spats significantly reduced flow detachment along the side surfaces, as seen in better-attached flow patterns and a smaller wake region.

Enhanced drag recovery was observed in the rear section of the front wheel arch, with lower pressure zones contributing to aerodynamic efficiency.

A larger low-velocity field beneath the vehicle with spats resulted in increased underbody pressure, leading to a notable reduction in downforce.

- **Outwash Effect:**

The spats generated a clear outwash effect, redirecting airflow behind the front wheels and along the vehicle's sides, reducing overall drag and improving stability.

- **Drawback of Lift Coefficient:**

The increase in underbody pressure caused by the spats led to a significant reduction in downforce ($\Delta C_L = -0.154$). This reduction in downforce may negatively impact the vehicle's high-speed stability and cornering performance, especially in scenarios where strong ground effect is critical.

Despite minor discrepancies due to geometric simplifications in the CFD model, the simulations provided accurate insights into the aerodynamic behavior. The findings highlight the efficacy of spats in optimizing aerodynamic resistance, demonstrating their potential for practical applications in vehicle design.